AIAA-2004-0655
Verification and Validation of Pseudospectral Shock Fitted Simulations of Supersonic Flow over a Blunt Body

G. P. Brooks
Air Force Research Laboratory
Wright-Patterson AFB, Ohio
and
J. M. Powers
Department of Aerospace and
Mechanical Engineering
University of Notre Dame
Notre Dame, Indiana

42nd AIAA Aerospace Sciences Meeting and Exhibit
5-8 January 2004 / Reno, NV

VERIFICATION AND VALIDATION OF PSEUDOSPECTRAL SHOCK FITTED SIMULATIONS OF SUPERSONIC FLOW OVER A BLUNT BODY *

Gregory P. Brooks †
Air Force Research Laboratory
Wright-Patterson Air Force Base, Ohio 45433

Joseph M. Powers‡
Department of Aerospace and Mechanical Engineering
University of Notre Dame
Notre Dame, Indiana 46556

Abstract

A highly accurate pseudospectral solver for the inviscid, supersonic flow of a calorically perfect ideal gas over arbitrary axisymmetric blunt body geometries is verified in its ability to approximate solutions to the Euler equations to within a dimensionless error tolerance of 10^{-12} in predictions of flow quantities and validated to within a dimensionless error tolerance of 10^{-2} in comparison of its predictions of shock location with experimental observation. In space, an exponential grid convergence rate in the $L_\infty[\Omega]$ error in density is predicted due to fitting of the detached bow shock and approximation of spatial derivatives via basis functions with global support; in contrast, a more standard shock capturing scheme will necessarily converge at only first order due to the corrupting influences of large numerical viscosity in the vicinity of the shock, rendering verification and validation more difficult. In time, casting the discrete form of the governing equations in the standard form $\frac{d\mathbf{x}}{dt} = \mathbf{q}(\mathbf{x})$ allows the use of a standard algorithm which enables high accuracy in time integration as well. Verification is accomplished by comparison with known exact solutions in appropriate limits, computation of the alignment of velocity vectors with entropy gradient vectors, computation of deviation of total enthalpy from its freestream value, as well as formal grid convergence studies. Validation is given by showing that shock shape predictions for flow over a sphere are in essential agreement with that observed in experiment. The ability of the method to capture unsteady flow phenomena, including low-amplitude high order harmonics, is demonstrated on the problem of a uni-modal planar acoustic wave interacting with an attached shock and downstream flow field.

Introduction

As a prerequisite for developing a new technique for shape optimization of bodies in supersonic flow, [1] not discussed here, we require a highly accurate flow solution technique. In the present work, a summary is given of a recently developed spatially pseudospectral, temporally high accurate numerical approximation to the solution for the supersonic, inviscid flow of a calorically perfect ideal gas over an axisymmetric blunt body. [2] The shock is fit since approximation of discontinuous solutions with high order polynomials exhibits the Gibbs phenomenon in the form of global oscillations in the solution. [3] Attempts to remove the oscillations by spectral filtering or by addition of artificial viscosity significantly reduces the accuracy of the numerical method. The more common alternative of shock capturing, while generally stable, non-oscillatory, though in some incarnations of daunting complexity, yields only first order spatial accuracy; common adaptive mesh refinement strategies may not always be useful in reducing this error. [4]

As a secondary motivation for generating high accuracy solutions, it is noted that there are outstanding questions regarding numerical and physical instabilities in multi-dimensional shock dynamics for which a solution with high spatial and temporal accuracy has value. Issues of shock stability remain

 This study has received primary support from the United States Air Force Palace Knight Program and additional support from Los Alamos National Laboratory.

†Research Scientist, Member AIAA.

‡Associate Professor, Associate Fellow AIAA.

controversial [5−12] since it is not clear which effects are real and which are numerical artifacts. Although shock stability will be investigated only in a rudimentary way in the current work, the shock fitting method used here is the most appropriate for addressing fundamental stability questions for inviscid flows due to the intrinsically low level of numerical viscosity inherent in the method. Furthermore, should a physical instability exist, one would like to have a numerical method with sufficient robustness to automatically select the time step so as to resolve the dynamics; because of the additional dynamic equations which arise from the unsteady shock wave, a simple CFL criterion is insufficient in the general case. Fortunately, the casting of the discretized governing equations into the form $\frac{d\mathbf{x}}{d\tau} = \mathbf{q}(\mathbf{x})$, as done here, allows the use of standard software packages which have automatic time step selection, precluding the necessity of an explicit condition for numerical stability.

The literature on solutions to the supersonic flow over blunt body geometries is briefly reviewed. Rusanov [13] and Hayes and Probstein [14] have given thorough reviews of early contributions, of which a few will be mentioned. Two methodologies for calculating solutions to the supersonic flow about a blunt body are the direct and inverse methods. In the direct method the body shape is specified, and then the shock shape and flow field are calculated. In the inverse method the shock shape is specified, and the body shape which would support that shock shape is calculated. At first, studies concerning the inverse problem were based on series expansion of the governing equations in the vicinity of the shock wave. [15] Later, numerical solutions to the inverse, supersonic blunt body problem were performed by Garabedian and Lieberstein [16] and Van Dyke. [17] Evans and Harlow [18] were the first to generate numerical solutions to the direct problem by integrating the unsteady Euler equations to a relaxed steady state solution. Moretti and Abbett [19] used finite differences and fitting of the shock to generate accurate solutions of the Euler equations about a blunt body; this laid the foundation for subsequent shock-fitting numerical schemes. Pseudospectral approximations to the Euler equations employing shock-fitting with spectral filtering were first performed by Hussaini, *et al.* [20] and without spectral filtering by Kopriva. [21] The numerical technique employed in the current paper builds on the work by Kopriva, [21,22] Brooks and Powers, [23,2] and Brooks. [24] The novelty of our recent work lies in 1) its use of high accuracy time integration, enabled by our employment of a new standardized formulation, and 2) its detailed verification and validation studies.

Next, pseudospectral methods are briefly reviewed. An early unified mathematical description of the theory of spectral and pseudospectral methods was given by Gottlieb and Orszag. [3] Significant advances occurred in the late 1970's and early 1980's and are well documented by Canuto, *et al.,* [25] with particular application to fluid dynamics. For a more recent review, see Gottlieb and Hesthaven. [26]

There does not appear to be complete consensus in the literature for the definition of pseudospectral; a definition is adopted here which we believe useful and consistent with that of Fornberg. [27] We define a pseudospectral method to be a collocation type of method of weighted residuals, as defined by Finlayson, [28] in which the error in the solution to the governing equations is driven to zero at collocation points; the flow quantities are represented in terms of global Lagrange interpolating polynomials defined at the collocation points. These interpolating polynomials are not orthogonal. The spatial derivatives of the flow quantities are then calculated by differentiating the Lagrange interpolating polynomials. Efficient algorithms for calculating derivatives of Lagrange interpolating polynomials on arbitrary grids can be found in Fornberg; [27] these algorithms were used in the current work.

A important property of the pseudospectral method is that approximations to derivatives have global support, making it equivalent to a finite difference or finite element scheme with a stencil that extends over the entire domain. As the number of points is increased, the size of the stencil grows, leading to a higher order accurate solution. In many cases the spatial accuracy will be equivalent to that of spectral methods. However, in contrast to spectral methods, pseudospectral methods need not employ orthogonal basis functions.

In this paper, formulation of the classical two-dimensional blunt body problem for a high accuracy numerical solution will be outlined. The numerical solution technique is then discussed. The remainder of the paper is then devoted to a demonstration of the verification, which connotes a correct solution to the underlying mathematical model, and validation, which connotes that the model's predictions are in concordance with experimental observation, of the model and solution technique. First the solution is verified for a steady Taylor-Maccoll flow over a sharp-nose cone for which an independent solution is available via solution of ordinary differential equations (ODEs) which result from a standard similarity transformation. Next a detailed verification and more limited validation are performed for the steady blunt body problem for which no independent solution ex-

ists. Last, the model is exercised in a unsteady mode by subjecting the Taylor-Maccoll flow to a uni-modal acoustic freestream disturbance. The inherent non-linearity of the problem insures that the uni-modal input will spawn a multi-modal output, and the high spatial and temporal accuracy of the method allows detection of high frequency output modes.

Governing Equations

The two-dimensional, axisymmetric Euler equations for a calorically perfect ideal gas are, in dimensionless form:

$$\frac{\partial \rho}{\partial t} + u\frac{\partial \rho}{\partial r} + w\frac{\partial \rho}{\partial z} + \rho\left(\frac{\partial u}{\partial r} + \frac{\partial w}{\partial z} + \frac{u}{r}\right) = 0, \quad (1)$$

$$\frac{\partial u}{\partial t} + u\frac{\partial u}{\partial r} + w\frac{\partial u}{\partial z} + \frac{1}{\rho}\frac{\partial p}{\partial r} = 0, \quad (2)$$

$$\frac{\partial w}{\partial t} + u\frac{\partial w}{\partial r} + w\frac{\partial w}{\partial z} + \frac{1}{\rho}\frac{\partial p}{\partial z} = 0, \quad (3)$$

$$\frac{\partial p}{\partial t} + u\frac{\partial p}{\partial r} + w\frac{\partial p}{\partial z} + \gamma p\left(\frac{\partial u}{\partial r} + \frac{\partial w}{\partial z} + \frac{u}{r}\right) = 0, \quad (4)$$

where ρ is density, p is pressure, u and w are the velocities in the radial and axial directions, respectively, r is the radial coordinate, z is the axial coordinate, t is time, and γ is the ratio of specific heats. The dimensional form for pressure, p^*, density, ρ^*, and r^* and z^* components of velocity, u^* and w^* respectively are recovered by the following equations,

$$p^* = pp^*_\infty, \quad (5)$$

$$\rho^* = \rho\rho^*_\infty, \quad (6)$$

$$u^* = u\sqrt{p^*_\infty/\rho^*_\infty}, \quad w^* = w\sqrt{p^*_\infty/\rho^*_\infty}, \quad (7)$$

where dimensional quantities are denoted by a $*$, and freestream quantities are denoted by ∞. The dimensional space and time variables are

$$z^* = zL, \quad r^* = rL, \quad (8)$$

$$t^* = tL/\sqrt{p^*_\infty/\rho^*_\infty}, \quad (9)$$

where L is the length of the body. The freestream flow is at zero angle of attack so that the component of freestream velocity in the r direction, $u_\infty = 0$.

Next, some secondary variables which will be useful in verification of the numerical solutions are considered. In this two-dimensional flow, the vorticity vector has only one non-zero component, which lies in the θ direction. It is

$$\omega_\theta = \frac{\partial u}{\partial z} - \frac{\partial w}{\partial r}. \quad (10)$$

Here the following scaling has been employed

$$\omega^*_\theta = \frac{1}{L}\sqrt{\frac{p^*_\infty}{\rho^*_\infty}}\omega_\theta. \quad (11)$$

Next, defining the entropy as s, one has, for a calorically perfect ideal gas with zero freestream entropy,

$$s = \ln\left(\frac{p}{\rho^\gamma}\right), \quad (12)$$

where the entropy is non-dimensionalized by the the specific heat at constant volume, c^*_v,

$$s^* = sc^*_v. \quad (13)$$

The total enthalpy H_o for the calorically perfect ideal gas is

$$H_o = \frac{\gamma}{\gamma - 1}\frac{p}{\rho} + \frac{1}{2}\left(u^2 + w^2\right). \quad (14)$$

In dimensional terms, the total enthalpy is

$$H^*_o = \frac{p^*_\infty}{\rho^*_\infty}H_o. \quad (15)$$

The temperature T is given by the ideal gas law

$$T = \frac{1}{\gamma - 1}\frac{p}{\rho}. \quad (16)$$

In dimensional terms, the temperature is

$$T^* = \frac{p^*_\infty}{c^*_v\rho^*_\infty}T. \quad (17)$$

Last, the Mach number M has its standard definition for the calorically perfect ideal gas:

$$M = \sqrt{\frac{u^2 + w^2}{\gamma\frac{p}{\rho}}}. \quad (18)$$

To facilitate the solution to the Euler equations for time-varying geometry, Eqs. $(1-4)$ are rewritten in terms of a general body-fitted coordinate system, $\xi(z,r,t)$, $\eta(z,r,t)$, and $\tau(z,r,t)$. Employing the chain rule of differentiation,

$$\begin{aligned}
\frac{\partial}{\partial z} &= \frac{\partial \xi}{\partial z}\frac{\partial}{\partial \xi} + \frac{\partial \eta}{\partial z}\frac{\partial}{\partial \eta} + \frac{\partial \tau}{\partial z}\frac{\partial}{\partial \tau}, \\
\frac{\partial}{\partial r} &= \frac{\partial \xi}{\partial r}\frac{\partial}{\partial \xi} + \frac{\partial \eta}{\partial r}\frac{\partial}{\partial \eta} + \frac{\partial \tau}{\partial r}\frac{\partial}{\partial \tau}, \\
\frac{\partial}{\partial t} &= \frac{\partial \xi}{\partial t}\frac{\partial}{\partial \xi} + \frac{\partial \eta}{\partial t}\frac{\partial}{\partial \eta} + \frac{\partial \tau}{\partial t}\frac{\partial}{\partial \tau},
\end{aligned} \quad (19)$$

and taking $\tau(z,r,t) = t$, the nondimensional form of Eqs. $(1-4)$ in generalized coordinates is

$$\begin{aligned}
&\frac{\partial \rho}{\partial \tau} + \widehat{u}\frac{\partial \rho}{\partial \xi} + \widehat{w}\frac{\partial \rho}{\partial \eta} + \frac{\rho u}{r} \\
&+\rho\left(\frac{\partial \xi}{\partial r}\frac{\partial u}{\partial \xi} + \frac{\partial \xi}{\partial z}\frac{\partial w}{\partial \xi} + \frac{\partial \eta}{\partial r}\frac{\partial u}{\partial \eta} + \frac{\partial \eta}{\partial z}\frac{\partial w}{\partial \eta}\right) = 0,
\end{aligned} \quad (20)$$

$$\frac{\partial u}{\partial \tau}+\widehat{u}\frac{\partial u}{\partial \xi}+\widehat{w}\frac{\partial u}{\partial \eta}+\frac{1}{\rho}\left(\frac{\partial \xi}{\partial r}\frac{\partial p}{\partial \xi}+\frac{\partial \eta}{\partial r}\frac{\partial p}{\partial \eta}\right)=0, \quad (21)$$

$$\frac{\partial w}{\partial \tau}+\widehat{u}\frac{\partial w}{\partial \xi}+\widehat{w}\frac{\partial w}{\partial \eta}+\frac{1}{\rho}\left(\frac{\partial \xi}{\partial z}\frac{\partial p}{\partial \xi}+\frac{\partial \eta}{\partial z}\frac{\partial p}{\partial \eta}\right)=0, \quad (22)$$

$$\frac{\partial p}{\partial \tau}+\widehat{u}\frac{\partial p}{\partial \xi}+\widehat{w}\frac{\partial p}{\partial \eta}+\frac{\gamma p u}{r}$$
$$+\gamma p\left(\frac{\partial \xi}{\partial r}\frac{\partial u}{\partial \xi}+\frac{\partial \xi}{\partial z}\frac{\partial w}{\partial \xi}+\frac{\partial \eta}{\partial r}\frac{\partial u}{\partial \eta}+\frac{\partial \eta}{\partial z}\frac{\partial w}{\partial \eta}\right)=0, \quad (23)$$

where the contravariant velocity components $\widehat{u}$ and $\widehat{w}$ are

$$\widehat{u}=\frac{\partial \xi}{\partial t}+u\frac{\partial \xi}{\partial r}+w\frac{\partial \xi}{\partial z}, \quad (24)$$

$$\widehat{w}=\frac{\partial \eta}{\partial t}+u\frac{\partial \eta}{\partial r}+w\frac{\partial \eta}{\partial z}. \quad (25)$$

The following standard relations between the metrics and inverse metrics are also necessary

$$\begin{aligned}
\frac{\partial \xi}{\partial z}&=\frac{1}{J}\frac{\partial r}{\partial \eta}, & \frac{\partial \eta}{\partial z}&=-\frac{1}{J}\frac{\partial r}{\partial \xi}, \\
\frac{\partial \xi}{\partial r}&=-\frac{1}{J}\frac{\partial z}{\partial \eta}, & \frac{\partial \eta}{\partial r}&=\frac{1}{J}\frac{\partial z}{\partial \xi}, \\
\frac{\partial \xi}{\partial t}&=\frac{\left(\frac{\partial r}{\partial \tau}\frac{\partial z}{\partial \eta}-\frac{\partial r}{\partial \eta}\frac{\partial z}{\partial \tau}\right)}{J}, & \frac{\partial \eta}{\partial t}&=\frac{\left(\frac{\partial r}{\partial \xi}\frac{\partial z}{\partial \tau}-\frac{\partial r}{\partial \tau}\frac{\partial z}{\partial \xi}\right)}{J}, \\
J&=\frac{\partial r}{\partial \eta}\frac{\partial z}{\partial \xi}-\frac{\partial r}{\partial \xi}\frac{\partial z}{\partial \eta}, & &
\end{aligned} \quad (26)$$

where J is the determinant of the metric Jacobian matrix.

Computational and Physical Coordinates

The physical domain of the blunt body problem, Fig. 1, is mapped to the computational domain, $\xi \in [0,1]$, $\eta \in [0,1]$, in such a way that the body surface lies along the computational boundary $(\xi,0)$, the shock lies along the boundary $(\xi,1)$, the symmetry axis is a third boundary at $(0,\eta)$, and the fourth boundary at $(1,\eta)$ is a supersonic outflow. The transformation between the physical coordinates (r,z) and computational coordinates (ξ,η) is taken to be

$$r(\xi,\eta,\tau)=R(\xi)+\frac{\eta\frac{dZ(\xi)}{d\xi}h(\xi,\tau)}{\sqrt{\left(\frac{dR(\xi)}{d\xi}\right)^2+\left(\frac{dZ(\xi)}{d\xi}\right)^2}}, \quad (27)$$

$$z(\xi,\eta,\tau)=Z(\xi)-\frac{\eta\frac{dR(\xi)}{d\xi}h(\xi,\tau)}{\sqrt{\left(\frac{dR(\xi)}{d\xi}\right)^2+\left(\frac{dZ(\xi)}{d\xi}\right)^2}}. \quad (28)$$

where the nonlinear function $h(\xi,\tau)$ must be specified to completely determine the mapping, and $R(\xi)$ and $Z(\xi)$ are known functions. After manipulation, the transformations in Eqs. (27) and (28) yield the following identity

$$h(\xi,\tau)=\sqrt{\left(z(\xi,1,\tau)-z(\xi,0,\tau)\right)^2+\left(r(\xi,1,\tau)-r(\xi,0,\tau)\right)^2}, \quad (29)$$

from which it is seen that the function $h(\xi,\tau)$ is the distance in $r-z$ space between the body surface, $\eta=0$, and the shock, $\eta=1$, along lines of constant ξ. The function $h(\xi,\tau)$ is subsequently referred to as the shock distance function. It is seen that Eqs. (27) and (28) form an implicit algebraic equation for the coordinate transformation. It is apparent from Eqs. (27) and (28) that the functions $R(\xi)$ and $Z(\xi)$ parameterize the blunt body surface, $\eta=0$, *i.e.*

$$\begin{aligned}
r(\xi,0,\tau)&=R(\xi), \\
z(\xi,0,\tau)&=Z(\xi),
\end{aligned} \quad (30)$$

and that the body surface is not a function of time. The transformations in Eqs. (27) and (28) have been constructed so that lines of constant ξ are normal to the body surface and have no curvature in $r-z$ space

The time evolution equations for the physical grid $r(\xi,\eta,\tau)$, and $z(\xi,\eta,\tau)$ can be found by differentiating Eqs. (27) and (28) with respect to time as follows,

$$\frac{\partial}{\partial \tau}r(\xi,\eta,\tau)=\frac{\eta\frac{dZ(\xi)}{d\xi}v(\xi,\tau)}{\sqrt{\left(\frac{dR(\xi)}{d\xi}\right)^2+\left(\frac{dZ(\xi)}{d\xi}\right)^2}}, \quad (31)$$

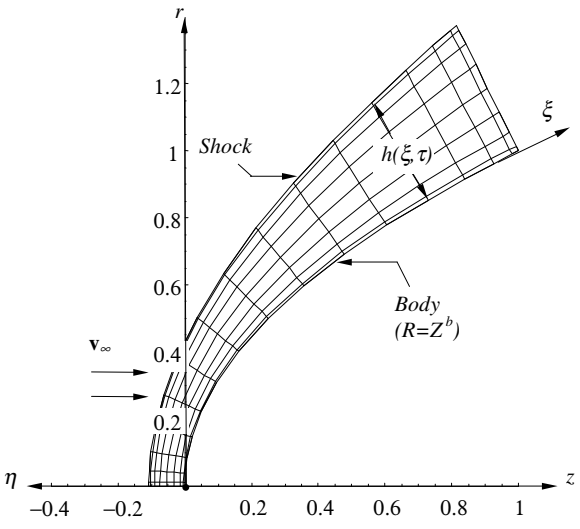

Figure 1: Schematic of shock-fitted high Mach number flow over an axisymmetric blunt body including computational (ξ,η) and physical (r,z) coordinates.

$$\frac{\partial}{\partial\tau}z\left(\xi,\eta,\tau\right)=-\frac{\eta\frac{dR(\xi)}{d\xi}v\left(\xi,\tau\right)}{\sqrt{\left(\frac{dR(\xi)}{d\xi}\right)^{2}+\left(\frac{dZ(\xi)}{d\xi}\right)^{2}}}, \qquad (32)$$

where the shock velocity function $v\left(\xi,\tau\right)$ is

$$v\left(\xi,\tau\right)=\frac{\partial}{\partial\tau}h\left(\xi,\tau\right). \qquad (33)$$

Boundary and Initial Conditions

Formulation of the boundary and initial conditions is a complex task, fully described in Ref. 2. In brief, at the body surface one enforces the kinematic constraint of zero mass flux. The inviscid model allows for a finite slip velocity at the body surface. At the shock, the usual Rankine-Hugoniot jump equations are enforced; this becomes a highly detailed task in the unsteady generalized coordinate system which must be employed for the shock fitting method. On the centerline, a Dirichlet condition on entropy, appropriate in either the steady state limit or the limit of an unsteady attached shock, is used. At the outflow, no physical boundary conditions are required as all waves are exiting the domain.

As an initial condition, the shock distance function is taken to be a constant, whose particular value is not relevant to the long time results. This allows specification of the grid coordinates in the initial state. Specification of an incoming Mach number, unperturbed flow quantities, and shock shape allows one to specify post-shock values of all physical variables via Rankine-Hugoniot relations. These values at the initial state are then simply projected as constants along lines of constant ξ. While the initial value problem is formally solved, the only concern here will be with results at times sufficiently long so that initial transients have relaxed, leaving either steady state or limit cycle behavior at long time.

Numerical Method

Here, the procedure for formulating this problem as a system of ODEs is outlined. The Euler equations, physical grid evolution equations, shock velocity equation, and boundary conditions defined over the computational domain

$$\Omega:\left\{\xi\in\left[0,1\right],\eta\in\left[0,1\right]\right\}, \qquad (34)$$

and bounded by S, can be written in the form of the following coupled system of time-dependent partial differential and algebraic equations

$$\frac{\partial\mathbf{y}}{\partial\tau}+\mathbf{f}\left(\mathbf{y},\frac{\partial\mathbf{y}}{\partial\xi},\frac{\partial\mathbf{y}}{\partial\eta}\right)=\mathbf{0}, \qquad (35)$$

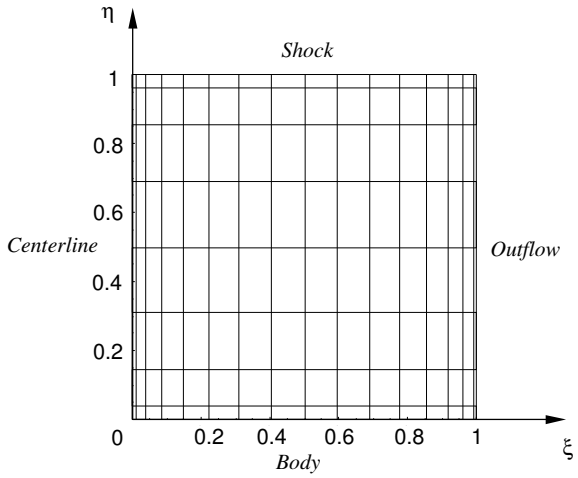

Figure 2: Computational grid for the shock-fitted blunt body.

$$\mathbf{g}\left(\mathbf{y},\frac{\partial\mathbf{y}}{\partial\xi},\frac{\partial\mathbf{y}}{\partial\eta}\right)=\mathbf{0}, \qquad (36)$$

along with the initial conditions,

$$\mathbf{y}\left(\xi,\eta,0\right)=\mathbf{y}_{0}\left(\xi,\eta\right), \qquad (37)$$

where ξ and η are independent spatial variables in the computational space, and $\mathbf{f}$ and $\mathbf{g}$ are nonlinear functions of the dependent variables $\mathbf{y}\left(\xi,\eta,\tau\right)$ and its spatial derivatives. All of the algebraic constraints, Eq. (36), are boundary conditions and thus apply only on S. A sketch of the domain in the transformed computational space is shown if Fig. 2. It was found [24] that the non-uniform grid shown in Fig. 2 gave rise to a more uniform error distribution in interpolating known functions, and so a grid of this class was used in all calculations reported here.

Approximating $\mathbf{y}\left(\xi,\eta,\tau\right)$ and its spatial derivatives via global Lagrange interpolating polynomials, as described in detail in Ref. 2, the system of partial differential and algebraic equations in Eqs. (35) and (36) reduce to the following system of P_2 differential-algebraic equations

$$\frac{dy_{p}\left(\tau\right)}{d\tau}=f_{p}\left(y_{1},...,y_{P_{2}}\right),\quad p=1,...,P_{1}, \qquad (38)$$

$$0=g_{p'}\left(y_{1},...,y_{P_{2}}\right),\quad p'=P_{1}+1,...,P_{2}, \qquad (39)$$

with initial conditions from Eq. (37)

$$y_{p}\left(0\right)=y_{0p},\quad p=1,...,P_{1}. \qquad (40)$$

Here $y_{1}\left(\tau\right),...,y_{P_{2}}\left(\tau\right)$ are the flow quantities, physical grid coordinates, and shock velocity evaluated at nodal points on an $\left(N+1\right)\times\left(M+1\right)$ mesh. In this

problem, it is possible through a detailed analysis to solve for the $y_{p'}(\tau)$, $p' = P_1 + 1, ..., P_2$, as explicit functions of the y_p, $p = 1, ..., P_1$, *i.e.*

$$y_{p'}(\tau) = \widehat{g}_{p'}(y_1, ..., y_{P_1}), \quad p' = P_1 + 1, ..., P_2, \quad (41)$$

so as to transform Eqs. (38) and (39) into the following system of P_1 ODEs,

$$\frac{dx_p(\tau)}{d\tau} = q_p(x_1, ..., x_{P_1}), \quad p = 1, ..., P_1, \quad (42)$$

where

$$q_p(x_1, ..., x_{P_1}) \equiv f_p(y_1, ..., y_{P_1}, \widehat{g}_{p'}(y_1, ..., y_{P_1})), \quad p = 1, ..., P_1, \quad p' = P_1 + 1, ..., P_2, \quad (43)$$

and

$$x_p(\tau) = y_p(\tau), \quad p = 1, ..., P_1. \quad (44)$$

The accompanying initial conditions are

$$x_p(0) = x_{0p}, \quad p = 1, ..., P_1. \quad (45)$$

In compact vector notation, Eq. (42) is

$$\frac{d\mathbf{x}}{d\tau} = \mathbf{q}(\mathbf{x}), \quad (46)$$

with accompanying initial conditions

$$\mathbf{x}(0) = \mathbf{x}_0, \quad (47)$$

from Eq. (45). After spatial discretization on an $(N+1) \times (M+1)$ grid, the equations become a system of $P_1 = 6NM + 2M$ ODEs.

Solutions have been obtained for Eqs. $(46 - 47)$ with the standard solver LSODA, [29,30] which automatically adjusts the time step to achieve a specified level of accuracy. It also automatically switches between an explicit method and implicit method depending on the stiffness of the problem. A typical steady state calculation on a 17×9 grid took 106 seconds CPU time on a single 800 MHz processor with 512 MB of RAM. For steady state problems, the criteria for stopping the integration is when the $L_\infty[\Omega]$ error in $\rho(\xi, \eta, \tau \to \infty)$ does not change appreciably.

Verification and Validation

Taylor-Maccoll Flow

The self-similar solution to supersonic flow over a cone, also known as the Taylor-Maccoll solution, [31] will be used to verify the algorithm described in the previous section. First, a highly accurate ODE solver is used to calculate the Taylor-Maccoll solution, which will be subsequently referred to as the exact solution. The only modification to the blunt body problem formulation to generate numerical approximations to the Taylor-Maccoll flow is to replace the centerline boundary condition at $\xi = 0$ with a Dirichlet boundary condition containing the values of ρ, u, w, p, r, and z taken from the exact solution. A schematic of a 40 degree cone including the physical and computational coordinates is shown in Figure 3 for a 5×5 grid for $M_\infty = 3.5$, $\rho_\infty = p_\infty = 1$. A value of $r_o = 0.1$ was chosen for the results presented in this section. The initial conditions for ρ, u, w, p, r, and z are taken from the exact solution, and a sinusoidal distribution is chosen for the initial shock velocity: $v(\xi, 0) = 0.1 \sin(2\pi\xi)$.

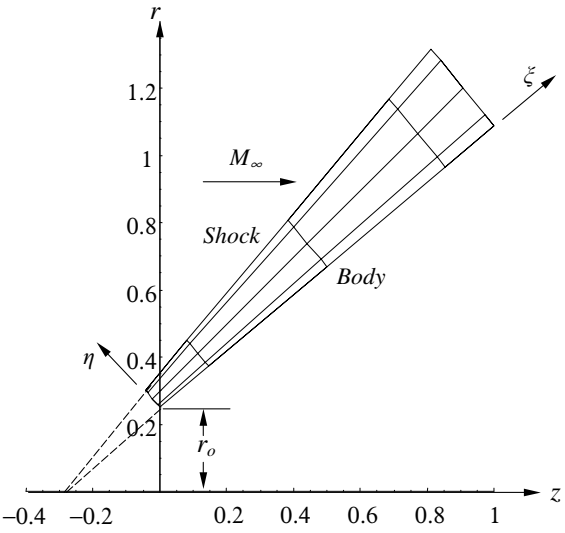

Figure 3: Schematic of the physical (r, z) and computational (ξ, η) grids for the Taylor-Maccoll problem.

In Fig. 4, the time history of the $L_\infty[\Omega]$ difference between the temporally local $\rho(\xi, \eta, \tau)$ values and steady, exact, Taylor-Maccoll values over the domain, Ω, for the pseudospectral prediction measured against the exact solution for a $M_\infty = 3.5$ flow over a 40 degree cone solved on a 5×17 grid is shown. The figure demonstrates a rapid relaxation which is approaching the exact solution; however, this only demonstrates relaxation in time, not in spatial grid resolution. For this grid the residual relaxes to a steady state value of 10^{-12}, which, since the base solution is exact, represents the true steady state error.

For spatial resolution, a grid convergence test for the pseudospectral prediction of the Taylor-Maccoll flow is conducted by refining the grid in the $\eta-$direction for a fixed number of five nodes in the

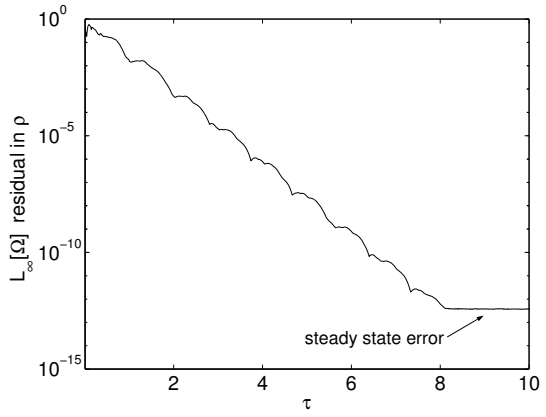

Figure 4: Single 5×17 grid $L_\infty[\Omega]$ residual difference in $\rho\,(\xi, \eta, \tau)$ measured against steady Taylor-Maccoll similarity solution as a function of time, τ, for a 40^o cone at $M_\infty = 3.5$.

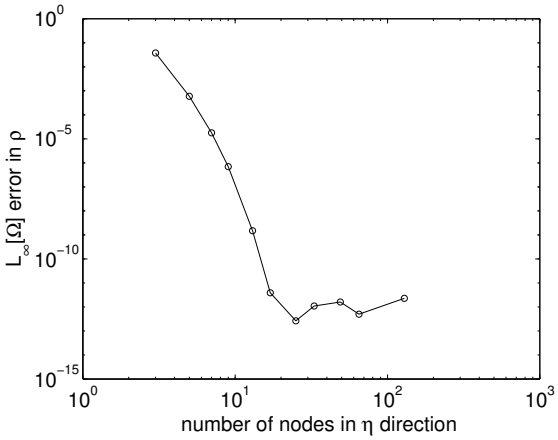

Figure 5: $L_\infty[\Omega]$ error in $\rho\,(\xi, \eta)$ measured against a Taylor-Maccoll similarity solution for a 40^o cone in $M_\infty = 3.5$ flow as grid is refined in the η direction.

$\xi-$direction. In these calculations, the time is sufficiently long so as to relax all transients. The accuracy of the method is unaffected by grid refinement in the $\xi-$direction since all derivatives are zero in that direction. As seen from Fig. 5, there is an ever-steeper decrease in the error until about 10^{-12} when the error flattens, probably due to roundoff effects. Note the spectral nature of the grid convergence, that is the slope of the error curve continues to steepen with increasing number of nodes, at least until the roundoff limit is reached, and does not reach a constant value for the slope as would be the case for a method with a fixed order of accuracy. Note also that remarkable accuracy is achieved with a grid which is extremely coarse by the standards of typical low-order finite difference or finite element calculations.

Steady State Flow over a Blunt Body

The following functions were chosen to parameterize the blunt body surface

$$R(\xi) = \xi, \tag{48}$$

$$Z(\xi) = \xi^{1/b}, \tag{49}$$

where the domain for the geometric parameter b is restricted to $b \in (0, 1)$. Eliminating the parameter ξ, it is seen that the body surface is described by $R = Z^b$. For $b = 0.5$, $M_\infty = 3.5$, $\rho_\infty = p_\infty = 1$, contour plots of Mach number and pressure are shown in Figs. 6 and 7. The results are obtained on a grid of dimension 17×9, again coarse by standards of finite difference or finite element calculations, but due to the high order of accuracy of the pseudospectral

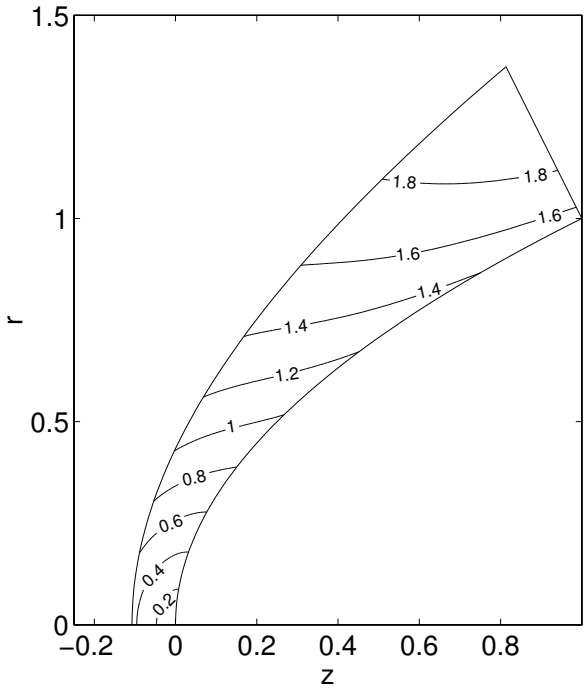

Figure 6: Contours of Mach number, M, for flow over the blunt body for $b = 0.5$, $M_\infty = 3.5$, 17×9 grid.

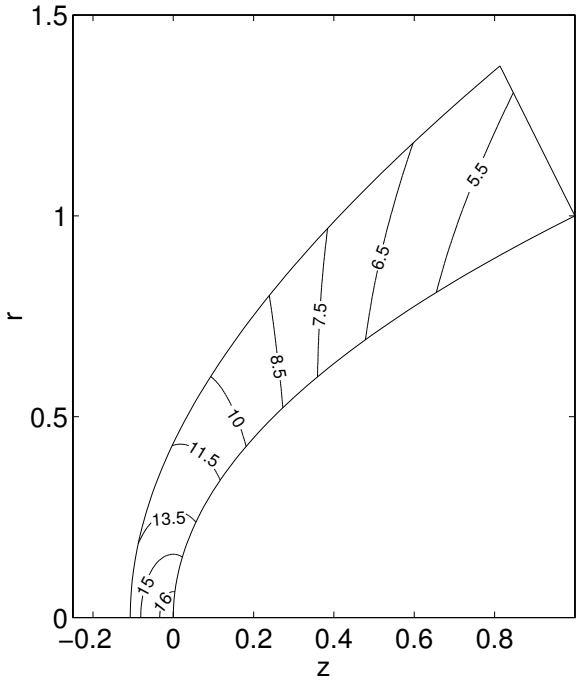

Figure 7: Contours of pressure p for flow over the blunt body for $b = 0.5$, $M_\infty = 3.5$, 17×9 grid.

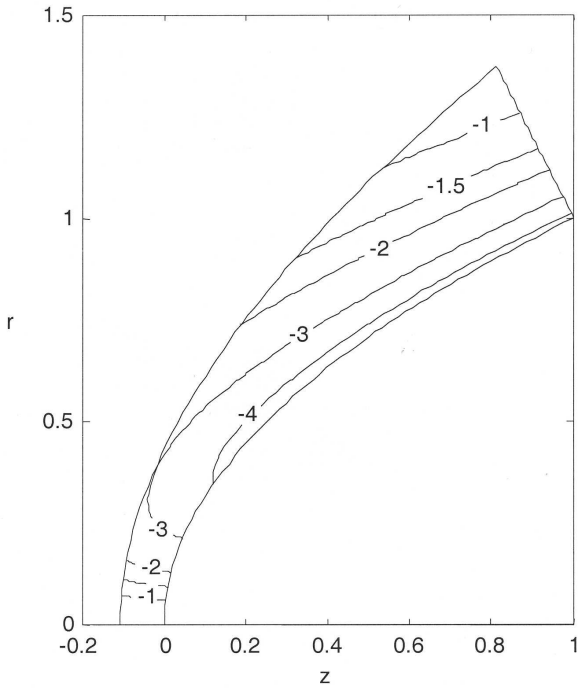

Figure 8: Contours of vorticity ω_θ for flow over the blunt body for $b = 0.5$, $M_\infty = 3.5$, 17×9 grid.

method, yields results which are remarkably precise. The sonic line, $M = 1$, is predicted in Fig. 6, as well as the fact that the outflow velocity is indeed supersonic as required in the derivation of the outflow boundary condition. In Fig. 7, the pressure at the stagnation point is seen to be more than sixteen times the freestream pressure at $M_\infty = 3.5$, and the jump in pressure across the normal shock at the centerline is over thirteen times the freestream pressure. The pressure weakens away from the stagnation point.

Contours of vorticity are shown in Fig. 8. Brooks [24] gives a detailed discussion of vorticity evolution, summarized here. In this flow there are four sources which induce changes of vorticity of a fluid particle: shock curvature, density changes of the fluid particle, baroclinic effects, and geometrical divergence. The shock curvature source can only be realized after a standard, but detailed, examination of the Rankine-Hugoniot jump conditions. The other three are revealed by the Helmholtz vorticity transport equation, a consequence of the governing mass, momenta, and energy equations, which reduces here, using the material derivative definition of $\frac{d}{dt} \equiv \frac{\partial}{\partial t} + u\frac{\partial}{\partial r} + w\frac{\partial}{\partial z}$, to the following

$$\frac{d\omega_\theta}{dt} = \frac{\omega_\theta}{\rho}\frac{d\rho}{dt} + \frac{1}{\rho^2}\left(\frac{\partial\rho}{\partial z}\frac{\partial p}{\partial r} - \frac{\partial\rho}{\partial r}\frac{\partial p}{\partial z}\right) + \omega_\theta\frac{u}{r}. \quad (50)$$

Because of the complex interplay of these mechanisms, it is difficult to attribute clear causality to all the effects represented in Fig. 8. It is noticed that in the far field, the magnitude of vorticity is decreasing. This is likely due to the diminished far-field body curvature, which induces diminished far-field shock curvature, and thus less entropy is generated at the shock.

While plots of pressure, Mach number, and vorticity are useful for qualitative understanding of the blunt body flow field, they are not good tools for formal verification of the numerical algorithm. To remedy this, a series of calculations which give a progressively better verification is presented in the following paragraphs.

As a rough means of verification, a comparison is made between the numerical results for the pressure distribution on the body with that of the modified Newtonian [32] sine squared law,

$$C_p = C_{po}\sin^2\phi, \quad (51)$$

where C_{po} is the pressure coefficient at the body stagnation point and ϕ is the local surface inclination angle measured with respect to the z axis. The pressure coefficient, C_p is defined as

$$C_p = \frac{p^* - p^*_\infty}{\frac{1}{2}\rho^*_\infty w^{*2}_\infty} = \frac{p\,(\xi, 0, \tau) - 1}{\frac{1}{2}\gamma M^2_\infty}. \quad (52)$$

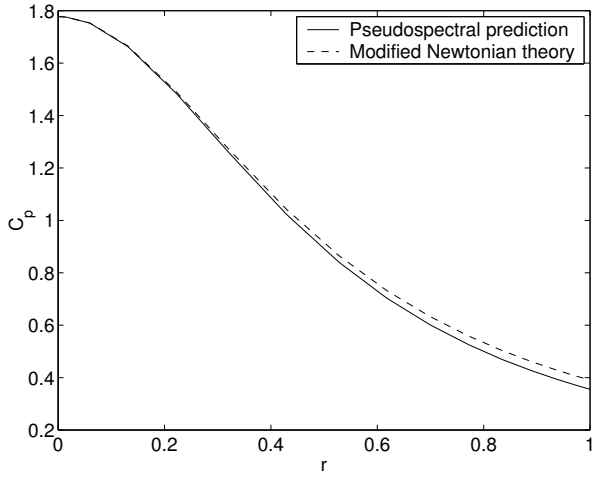

Figure 9: Blunt body surface C_p distribution predictions at $M_\infty = 3.5$ from modified Newtonian theory and from the pseudospectral method, where $b = 0.5$; 17×9 grid.

The modified Newtonian approximation is a semi-analytical model for the surface pressure distribution over blunt bodies. Anderson [33] reports that for a power law body with $b = 0.5$ and aspect ratio near unity, the modified Newtonian approximation does well in predicting the pressure distribution on the surface of the body. As can be seen from Fig. 9, the pseudospectral algorithm also predicts close agreement for the pressure distribution on the surface of the body defined by $R = \sqrt{Z}$.

Simultaneous consideration of entropy and velocity fields gives a better indication of verification. Contours of entropy along with the velocity vector field are shown in Fig. 10. Brooks [24] gives a standard discussion of how, in the limits of this study, the energy equation can be recast as

$$\frac{ds}{dt} = 0. \tag{53}$$

That is, the entropy of a fluid particle does not change along a streamline. Equation (53) is valid in smooth regions of the flow, but not across discontinuities, through which the second law of thermodynamics demands that entropy must increase. A fluid particle traveling on the axis of symmetry encounters a purely normal shock, which relative to other portions of the shock, is strongest, and is endowed with the maximum entropy of the flow field. Fluid particles away from the centerline encounter a weaker shock and acquire less entropy, in some proportion to their distance from the centerline. This is evident in Fig. 10. Also evident in Fig. 10 is the fact that the velocity vectors are parallel to lines of constant entropy.

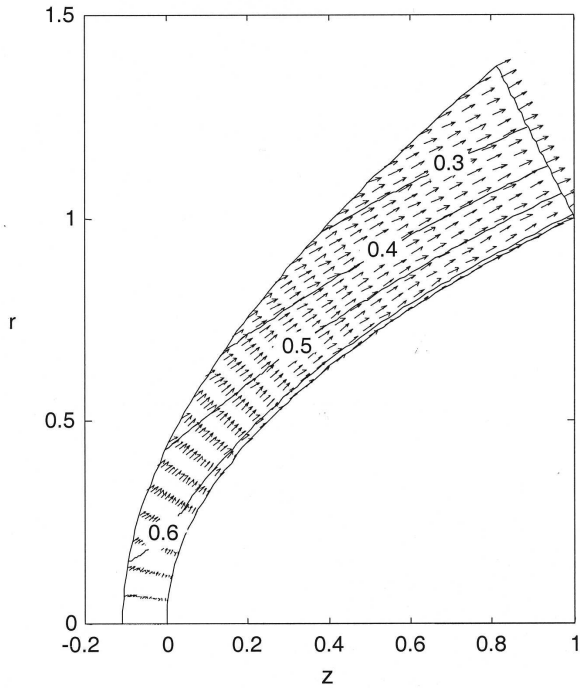

Figure 10: Contours of entropy s and velocity vectors for flow over the blunt body for $b = 0.5$, $M_\infty = 3.5$, 17×9 grid.

This is consistent with Eq. (53) in the long-time limit, which holds that the dot product of the velocity vector with the entropy gradient vector is zero. This was confirmed formally in a grid refinement study, not reported here.

Another more rigorous means of verifying the algorithm is by considering the variation of total enthalpy. In an extended analysis given by Brooks, [24] a relation is recovered, equivalent to that of Emanuel, [34] that for an inviscid flow

$$\frac{dH_o}{dt} = T\frac{ds}{dt} + \frac{1}{\rho}\frac{\partial p}{\partial t}. \tag{54}$$

This is a general, but not widely used, result. The less general, related, and widely used Crocco's equation, which appears in many forms in many sources, is insufficient for purposes of this study. Equation (54) simplifies further in the present problem. Here, Eq. (53) can be used to eliminate the material derivative of entropy at all times, and it is assumed pressure transients relax to zero in the long time limit, to get

$$\frac{dH_o}{dt} = 0, \qquad \text{as} \qquad t \to \infty. \tag{55}$$

Equation (55) holds that total enthalpy does not vary for a fluid particle, but that it may vary from streamline to streamline. However, when it is realized that

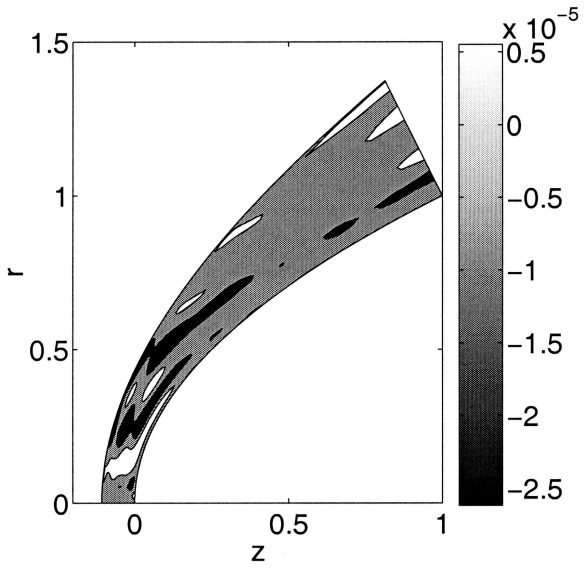

Figure 11: Contours of the difference between total enthalpy and its freestream value, $H_o - H_{o,\infty}$, for flow over the blunt body for $b = 0.5$, $M_\infty = 3.5$, 17×9 grid.

the unshocked flow has a spatially uniform value of total enthalpy, and that the Rankine-Hugoniot jump equations allow no change in total enthalpy through a discontinuity, it is seen that the flow of this study has the remarkable property that the total enthalpy is a spatially uniform constant in the long time limit. Thus, as long as the flow is stable, in the long time limit the difference of the local value of total enthalpy and its freestream value will formally be zero, and a plot of the difference gives a measure of the error distribution. Mathematically, it can be shown that the in the long time limit, the linear mometa equation has a first integral, with the constant of integration given by the unshocked freestream value. This algebraic relation, and its connection with total enthalpy for the calorically perfect ideal gas is found to be

$$\underbrace{\frac{\gamma}{\gamma-1}\frac{p}{\rho}+\frac{1}{2}\left(u^2+w^2\right)}_{H_o}=\underbrace{\frac{\gamma}{\gamma-1}+\frac{\gamma}{2}M_\infty^2}_{H_{o,\infty}}. \qquad (56)$$

Eq. (56) holds that the local value of total enthalpy H_o always maintains its preshock value of $H_{o,\infty}$. Contours of this difference $H_o - H_{o,\infty}$ are shown in Fig. 11. For this coarse 17×9 grid, the differences are on the order of 10^{-5}, a notably small value. Brooks [24] shows that when this grid resolution is increased to 29×15, the differences reduce to the order of 10^{-9}, and the error distribution is striated in bands roughly parallel to the body and shock surfaces.

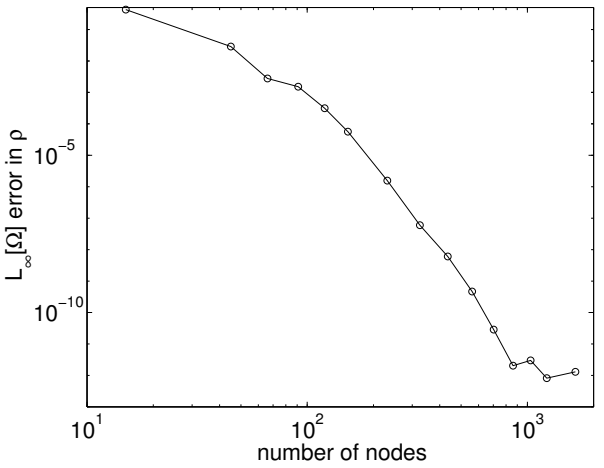

Figure 12: Grid convergence $L_\infty[\Omega]$ error in $\rho\,(\xi, \eta, \tau \to \infty)$ measured against a baseline, 65×33 grid, solution for a $b = 0.5$, $M_\infty = 3.5$ blunt body.

The most rigorous verification is given by a grid convergence study for the blunt body with the $L_\infty[\Omega]$ error over the domain, Ω in $\rho\,(\xi, \eta, \tau \to \infty)$ shown in Fig. 12, at $M_\infty = 3.5$ and $b = 0.5$, where the error is measured against a 65×33 or 2145 node numerical solution. For 861 nodes, the $L_\infty[\Omega]$ error over the domain, Ω in $\rho\,(\xi, \eta, \tau \to \infty)$ has been reduced to the order of 10^{-12} and subsequently flattens due to roundoff error. Like grid convergence plots for the Taylor-Maccoll solution, the convergence of the error for the blunt body problem shows a spectral convergence rate as expected of the pseudospectral numerical technique.

Last, to validate the model, in Fig. 13 a comparison is made of the pseudospectral prediction for the shock shape for $M_\infty = 3.5$ flow over a sphere with that of an empirical formula by Billig [35] developed for flow over spherically blunted cones based on experiment. It is obvious that the predictions match the experiments closely; here, the dimensionless difference between the predicted and measured shock position is roughly 10^{-2}. It is not clear how much error is present in the experimental results, which could include error from an imperfect curve fit to the data as well as intrinsic measurement errors.

Acoustic Interaction with Attached Shock

Here, a fundamentally unsteady problem is considered: the interaction of an unsteady, planar acoustic wave with an attached shock, for which the automatic time step selection in LSODA is critical in enabling one to have tight control over the error in the solution. In this case, neither verification nor validation

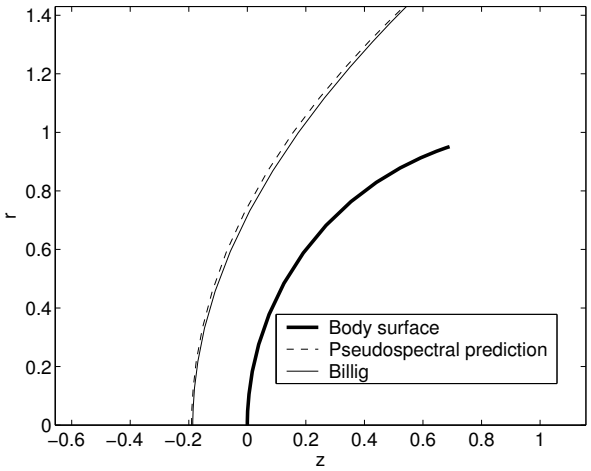

Figure 13: Shock shape prediction of the pseudospectral algorithm for a sphere $M_\infty = 3.5$ compared with an empirical formula by Billig [35] derived from experiments; 17×9 grid.

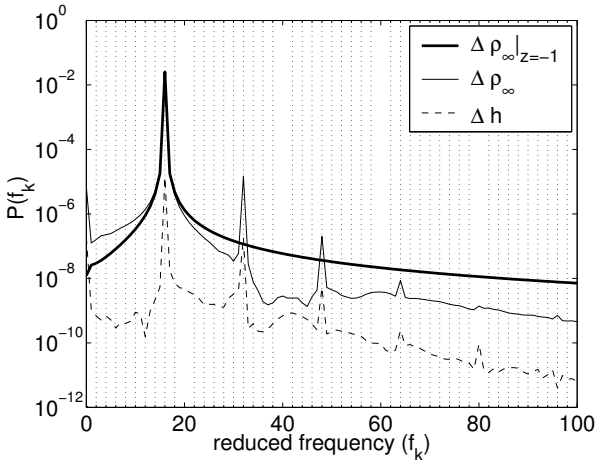

Figure 14: Frequency spectrum at a single point on the shock ($\xi = 1$), of the fluctuations in freestream density, $\Delta\rho_\infty = \rho_\infty - 1$, and the response of the shock, $\Delta h = h(1,t) - h_\infty(1)$. $M_\infty = 3.5$; 33×17 grid.

will be attempted; instead, results will be examined, and the accuracy of the method will be exploited to predict features which are more difficult to discern with lower order methods. A schematic of the grid is shown in Fig. 3, where $r_o = 0.01$ is chosen for this problem. The value of the freestream flow quantities ρ_∞, u_∞, w_∞, p_∞ at the shock are taken to be

$$\rho_\infty = -\frac{1}{2\sqrt{\gamma}}\left(F\left(\xi,\tau\right) - G\left(\xi,\tau\right)\right), \tag{57}$$

$$u_\infty = 0, \tag{58}$$

$$w_\infty = \frac{1}{2}\left(F\left(\xi,\tau\right) + G\left(\xi,\tau\right)\right), \tag{59}$$

$$p_\infty = 1 + \gamma\left(\rho_\infty - 1\right), \tag{60}$$

where

$$F\left(\xi,\tau\right) = \sqrt{\gamma}(M_\infty - 1), \tag{61}$$

$$G\left(\xi,\tau\right) = \sqrt{\gamma}(M_\infty + 1) \times(1 + \epsilon \sin\kappa(z(\xi,1,\tau) - \sqrt{\gamma}(M_\infty + 1)\tau)). \tag{62}$$

Choosing $\epsilon = 0.01$, $\kappa = 6\pi$, $M_\infty = 3.5$, and $\gamma = 1.4$ in Eqs. (61) and (62), the system of ODEs in Eq. (42) are integrated in time for $\tau \in [0,2]$ on a 33×17 grid. The CPU time for the calculation on a single 800 MHz processor was 7.5 hours. The initial conditions were set to the Taylor-Maccoll solution of the unperturbed freestream flow conditions, *i.e.* $\rho_\infty = 1$, $u_\infty = 0$, $w_\infty = \sqrt{\gamma}M_\infty$, $p_\infty = 1$. The relative and absolute error tolerances for the time integration were set to 10^{-10} and 10^{-12} respectively in LSODA.

Now, analyze the motion of a single point on the shock located at $\xi = \eta = 1$. The power spectrum, $P(f)$, as a function of reduced frequency for the perturbation in freestream density, $\Delta\rho_\infty = \rho_\infty - 1$, and shock distance function, $\Delta h = h(1,t) - h_\infty(1)$, at the point $\xi = \eta = 1$ are presented in Fig. 14 as well as $\Delta\rho_\infty|_{z=-1}$, which is well upstream of the shock. Initial transients in the solution are neglected in the estimation of the power spectrum by considering only $\tau \in [1.001, 2]$, so that the time interval is, $T = 0.999$.

The power spectrum, Fig. 14, clearly shows a large peak for $\Delta\rho_\infty|_{z=-1}$ at a reduced frequency of the driving disturbance of $f_{16} = \frac{\kappa}{2\pi}\sqrt{\gamma}(M_\infty + 1) = 16.0$, according to Eq. (42). Peaks in the power spectrum of Δh, and $\Delta\rho_\infty$ also appear at $f_{16} = 16.0$ in response to the frequency of oscillation of $\Delta\rho_\infty|_{z=-1}$. In addition, higher harmonics at integer multiples of the $f_{16} = 16.0$ forcing frequency are present in the power spectrum of Δh and $\Delta\rho_\infty$. The high accuracy of the current method is critical in capturing the correct shock dynamics for such small amplitude fluctuations, and in predicting the higher harmonics of the shock fluctuations in Fig. 14, where the amplitude of the power spectrum drops orders of magnitude with each successive harmonic. The current method is able to resolve up to the fourth harmonic of Δh, whose amplitude in the power spectrum is on the order of 10^{-10}.

Discussion

In this study, a description has been given of a

pseudospectral numerical approximation technique for the inviscid supersonic flow over a blunt body geometry in which the discretized form of the governing equations and boundary conditions are formulated in terms of a system of ODEs which can be solved using a standard solver. This formulation takes advantage of the strengths of widely available ODE solvers to generate time accurate solutions within prescribed error tolerances through automatic time step selection. Additionally, fitting of the shock and the use of basis functions which have global support in the solution approximation, permit high accuracy steady state approximations with relatively modest computational resources; a solution with an error of 10^{-5} can be obtained in 10^2 s on a single 800 MHz processor. This formulation has important potential applications such as approximating unsteady shock phenomena with sufficient accuracy to discern between physical versus numerical instabilities.

In problems such as those considered here, in which the topology of the discontinuity is simple, a high order of accuracy of convergence can be achieved. In problems with richer geometry, it is not realistic to expect to explicitly fit all discontinuities; one must then be satisfied with capturing the discontinuities with methods which have first order convergence. For such problems, even the most exotic technique which has a high order accuracy for smooth problems will necessarily converge only at first order. In examining the compressible aerodynamics literature, it is not always clear that this point is manifest, but it is clear that elucidating the results of any calculation in compressible aerodynamics with the techniques of verification and validation will yield consequent fruits in reliability, robustness, and general understanding.

In closing, a comment is given which has obvious generality beyond compressible aerodynamics. Consistent with the results typical in the discipline of verification and validation, following the employment of appropriate techniques, it is possible to verify a solution to a particular set of model equations, here the Euler equations, to a much higher degree of accuracy, here 10^{-12}, than to which it is possible to validate the model, here 10^{-2}. This does not suggest less accurate numerical methods should be used; in fact once the method is in place, it is easy in this case to generate high accuracy solutions. It simply suggests that one factor, numerical discretization error, has been effectively removed from consideration in developing a theory which explains the discrepancy between predictions and measurements. The more challenging problem is to determine which of many potential factors, *e.g.* neglect of physical mechanisms, inaccurate constitutive data, inaccurate measurements, best explains the discrepancy which remains.

References

[1] Brooks, G. P., and Powers, J. M., "A Karhunen-Loève Least-Squares Technique for Optimization of Geometry of a Blunt Body in Supersonic Flow," *Journal of Computational Physics*, (in press, 2004).

[2] Brooks, G. P., and Powers, J. M., "Standardized Pseudospectral Formulation of the Inviscid Supersonic Blunt Body Problem," *Journal of Computational Physics*, (in press, 2004).

[3] Gottlieb, D. and Orszag, S., *Numerical Analysis of Spectral Methods: Theory and Applications*, SIAM-CBMS, Philadelphia, 1977.

[4] Yamaleev, N. K., and Carpenter, M. H., "On Accuracy of Adaptive Grid Methods for Captured Shocks," *Journal of Computational Physics*, Vol. 181, No. 1, 2002, pp. 280-316.

[5] D'yakov, S. P., "On the Stability of Shock Waves," *Zhurnal Eksperimental'noi i Teoreticheskoi Fiziki*, Vol. 27, 1954, pp. 288-295.

[6] Kontorovich, V. M., "Concerning the Stability of Shock Waves," *Soviet Physics JETP*, Vol. 6, 1957, pp. 1179-1180.

[7] Quirk, J. J., "A Contribution to the Great Riemann Solver Debate," *International Journal for Numerical Methods in Fluids*, Vol. 18, No. 6, 1994, pp. 555-574.

[8] Bates, J. W., and Montgomery, D. C., "The D'yakov Instability of Shock Waves in Real Gases," *Physical Review Letters*, Vol. 84, No. 6, 2000, pp. 1180-1183.

[9] Robinet, J.-Ch., Gressier, J., Casalis, G., and Moschetta, J.-M., "Shock Wave Instability and the Carbuncle Phenomenon: Same Intrinsic Origin?," *Journal of Fluid Mechanics*, Vol. 417, 2000, pp. 237-263.

[10] Gressier, J., and Moschetta, J.-M., "Robustness Versus Accuracy in Shock-Wave Computations," *International Journal for Numerical Methods in Fluids*, Vol. 33, No. 3, 2000, pp. 313-332.

[11] Coulombel, J.-F., Benzoni-Gavage, S., and Serre, D., "Note on a Paper by Robinet, Gressier, Casalis & Moschetta," *Journal of Fluid Mechanics*, Vol. 469, 2002, pp. 401-405.

[12] Kim, S. S., Kim, C., Rho, O. H., and Hong, S. K., "Cures for the Shock Instability: Development of a Shock-Stable Roe Scheme," *Journal of Computational Physics*, Vol. 185, No. 2, 2003, pp. 342-374.

[13] Rusanov, V. V., "A Blunt Body in a Supersonic Stream," *Annual Review of Fluid Mechanics*, Vol. 8, 1976, pp. 377-404.

[14] Hayes, W. D., and Probstein, R. F., *Hypersonic Flow Theory, Vol. 1, Inviscid Flows*, Academic Press, New York, 1966.

[15] Lin, C. C., and Rubinov, S. I., "On the Flow Behind Curved Shocks," *Journal of Mathematics and Physics*, Vol. 27, 1948, pp. 105-129.

[16] Garabedian, P. R., and Lieberstein, H. M., "On the Numerical Calculation of Detached Bow Shock Waves in Hypersonic Flow," *Journal of the Aeronautical Sciences*, Vol. 25, No. 1, 1958, pp. 109-118.

[17] Van Dyke, M. D., "The Supersonic Blunt-Body Problem - Review and Extension," *Journal of the Aero/Space Sciences*, Vol. 25, No. 4, 1958, pp. 485-496.

[18] Evans, M. W., and Harlow, F. H., "Calculation of Supersonic Flow Past an Axially Symmetric Cylinder," *Journal of the Aeronautical Sciences* Vol. 25, No. 1, 1958, p. 269.

[19] Moretti, G., and Abbett, M., "A Time-Dependent Computational Method for Blunt Body Flows," *AIAA Journal* Vol. 4, No. 12, 1966, pp. 2136-2141.

[20] Hussaini, M. Y., Kopriva, D. A., Salas, M. D., and Zang, T. A., "Spectral Methods for the Euler Equations: Part 2. Chebyshev Methods and Shock-Fitting," *AIAA Journal* Vol. 23, No. 2, 1985, pp. 234-240.

[21] Kopriva, D. A., Zang, T. A., and Hussaini, M. Y., "Spectral Methods for the Euler Equations: The Blunt Body Problem Revisited," *AIAA Journal* Vol. 29, No. 9, 1991, pp. 1458-1462.

[22] Kopriva, D. A., "Shock-Fitted Multidomain Solution of Supersonic Flows," *Computer Methods in Applied Mechanics and Engineering*, Vol. 175, Nos. 3-4, 1999, pp. 383-394.

[23] Brooks, G. P., and Powers, J. M., "A Karhunen-Loève Galerkin Technique with Shock-Fitting for Optimization of a Blunt Body Geometry," AIAA Paper 2002-3861, 2002.

[24] Brooks, G. P., "A Karhunen-Loève Least-Squares Technique for Optimization of Geometry of a Blunt Body in Supersonic Flow," Ph.D. Dissertation, University of Notre Dame, Notre Dame, Indiana, 2003.

[25] Canuto, C., Hussaini, M. Y., Quarteroni, A., and Zang, T. A., *Spectral Methods in Fluid Dynamics*, Springer-Verlag, New York, 1988.

[26] Gottlieb, D., and Hesthaven, J. S., "Spectral Methods for Hyperbolic Problems," *Journal of Computational and Applied Mathematics*, Vol. 128, Nos. 1-2, 2001, pp. 83-131.

[27] Fornberg, B., *A Practical Guide to Pseudospectral Methods*, Cambridge University Press, Cambridge, 1998.

[28] Finlayson, B. A., *The Method of Weighted Residuals and Variational Principles*, Academic Press, New York, 1972.

[29] Hindmarsh, A. C., ODEpack, A Systematized Collection of ODE Solvers, in: Scientific Computing, R.S. Stepleman, *et al.* (eds.), North Holland, Amsterdam, 1983, pp. 55-64.

[30] Petzold, L., "Automatic Selection of Methods for Solving Stiff and Nonstiff Systems of Ordinary Differential Equations," *SIAM Journal on Scientific and Statistical Computing* Vol. 4, No. 1, 1983, pp. 136-148.

[31] Taylor, G. I., and Maccoll, J. W., "The Air Pressure on a Cone Moving at High Speeds, I and II," *Proceedings of the Royal Society of London*, Ser. A Vol. 139, No. 838, 1933, pp. 278-311.

[32] Lees, L., Hypersonic Flow, in: Proceedings of the Fifth International Aeronautical Conference, Los Angeles, Institute of the Aeronautical Sciences, New York, 1955, pp. 241-276.

[33] Anderson, J. D., *Hypersonic and High Temperature Gas Dynamics*, McGraw-Hill, New York, 1989.

[34] Emanuel, G., *Analytical Fluid Dynamics*, CRC Press, Boca Raton, Florida, 1994.

[35] Billig, F. S., "Shock-Wave Shapes Around Spherical and Cylinder-Nosed Bodies," *Journal of Spacecraft and Rockets*, Vol. 4, No. 6, 1967, pp. 822-823.